

DAGLFNet: Deep Feature Attention Guided Global and Local Feature Fusion for Pseudo-Image Point Cloud Segmentation

CHUANG CHEN ¹, YI LIN ², BO WANG ¹, JING HU ¹, XI WU ¹, AND WENYI GE^{1,*}

¹College of Computer Science, Chengdu University of Information Technology, Chengdu 610225, China;

²College of Computer Science, Sichuan University, Chengdu, 610065, China;

^{*}gewenyi15@cuit.edu.cn

Abstract: Environmental perception systems are crucial for high-precision mapping and autonomous navigation, with LiDAR serving as a core sensor providing accurate 3D point cloud data. Efficiently processing unstructured point clouds while extracting structured semantic information remains a significant challenge. In recent years, numerous pseudo-image-based representation methods have emerged to balance efficiency and performance. However, these methods often overlook the structural and semantic details of point clouds, leading to limited feature fusion and discriminability. This work proposes DAGLFNet, a pseudo-image-based semantic segmentation framework designed to extract discriminative features. It incorporates three key components: first, a Global-Local Feature Fusion Encoding (GL-FFE) module to enhance intra-set local feature correlation and capture global contextual information; second, a Multi-Branch Feature Extraction (MB-FE) network to capture richer neighborhood information and improve the discriminability of contour features; and third, a Feature Fusion via Deep Feature-guided Attention (FFDFA) mechanism to refine cross-channel feature fusion precision. Experimental evaluations demonstrate that DAGLFNet achieves mean Intersection-over-Union (mIoU) scores of 69.9% and 78.7% on the validation sets of SemanticKITTI and nuScenes, respectively. The method achieves an excellent balance between accuracy and efficiency, demonstrating strong potential for LiDAR-based applications.

1. Introduction

Semantic segmentation has become a cornerstone technology for 3D environmental perception, enabling dense semantic annotation and feature learning from LiDAR point clouds [1–3]. By providing structured interpretations of complex environments, this capability is fundamental to applications like robotics and autonomous driving. Modern LiDAR sensors capture tens of millions of points per second, allowing an unprecedentedly detailed representation of the surrounding 3D structure [4, 5]. However, the central challenge lies in developing effective strategies to process inherently unstructured and unordered point cloud data to extract discriminative features for reliable perception.

Current LiDAR segmentation techniques employ several distinct paradigms for handling point cloud data. Point-based methods process raw point sets directly, enabling dense feature interaction but relying on computationally intensive neighborhood searches to capture local geometric structures [6–8]. This results in significant resource demands, limiting scalability in large outdoor environments. Voxel-based methods discretize point clouds into regular volumetric grids and apply sparse convolutions for feature extraction [9–12]. However, the cubic growth of memory consumption with resolution makes high-resolution voxel grids prohibitively expensive to construct and process. Hybrid strategies integrating features from multiple representational domains have shown improved predictive accuracy [13]. Nevertheless, their heavy computational burden and challenges in system robustness remain significant obstacles for further improvement.

In recent years, range-view-based semantic segmentation of point clouds has garnered increasing

attention due to its favorable balance between computational efficiency and segmentation accuracy [3, 30]. By projecting irregular and complex LiDAR point clouds onto structured two-dimensional representations (such as range images), this approach enables more effective organization and encoding of spatial information, extraction of local and global features [17, 18], and offers several significant advantages. The regular image grids greatly simplify neighborhood queries and local feature aggregation, while avoiding costly and time-consuming three-dimensional operations, and have achieved encouraging performance. However, this projection strategy inevitably leads to depth conflict phenomena, where multiple 3D points are mapped to the same 2D pixel coordinates. This causes subsequent projected points to overwrite previously mapped points, resulting in an irreversible loss of 3D spatial structural information.

Recent methods have addressed the inherent depth conflicts and 3D information loss in direct range image projection by converting point clouds into pseudo-images. These methods aggregate and encode local 3D point clusters into 2D grid representations and fuse point features with 2D features to preserve complete point cloud information [14, 15], the segmentation results are shown in Fig. 1b. However, points from distinct semantic categories may be assigned to the same subregion during point cloud partitioning, causing inconsistent grouping that destabilizes local feature encoding and diminishes the expressive value of segmented regions. Furthermore, projecting features of these local point sets into 2D images compresses high-dimensional geometric details into abstract representations, leading to blurred boundaries and loss of fine-grained structural information. This exacerbates semantic ambiguity and feature degradation, as shown in Fig. 1a. Additionally, coarse fusion of 2D image features with original point cloud representations can introduce redundant or conflicting information, limiting the discriminative capacity and fidelity of point-wise features. These issues are particularly pronounced in distant, sparse, or occluded regions, where projected subregions often contain insufficient valid points, resulting in a significant decline in the structural fidelity of the pseudo-image representation.

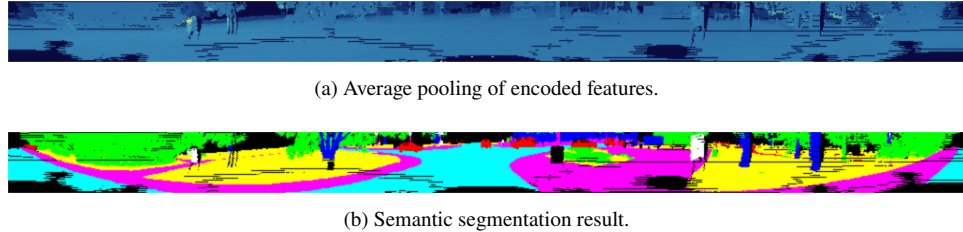


Fig. 1. (a) Visualization of feature ambiguity and boundary blurring through average pooling of encoded feature channels from the LiDAR point cloud representation, and (b) corresponding semantic segmentation result demonstrating the classification performance.

To address these challenges, we propose DAGLFNet, a novel framework integrating global-local feature aggregation, multi-branch feature extraction, and a deep feature-guided fusion mechanism. This design achieves a favorable balance between accuracy and computational efficiency for pseudo-image-based point cloud semantic segmentation. Specifically, local point sets generated by azimuth and laser-beam-based sub-region partitioning often exhibit significant internal geometric variability, undermining local feature representation stability. To address this and enhance local geometric consistency, we propose a Global-Local Feature Fusion Encoding (GL-FFE) module capable of simultaneously capturing global contextual dependencies and fine-grained local geometric relationships. During the mapping of point cloud subsets to image representations, boundary features are often blurred and susceptible to interference from adjacent regions. To overcome this limitation, we propose a Multi-Branch Feature Extraction (MB-FE) network designed to expand the receptive field and enhance the discriminative representation of

boundary features. Additionally, we introduce a Feature Fusion via Deep Feature-guided Attention (FFDFA) strategy during feature integration, which explicitly leverages distance information as a weighting constraint to refine cross-channel feature fusion precision.

In summary, our main contributions are as follows:

1. We introduce DAGLFNet, a novel network architecture for LiDAR point cloud semantic segmentation. Within this framework, geometric features are tightly integrated with 2D pseudo-image representations, enabling efficient processing of unstructured point data while fully capturing discriminative point-wise features.
2. We propose a comprehensive feature enhancement strategy comprising three key modules: (i) a GL-FFE module to capture long-range dependencies and stabilize local geometric representations; (ii) a MB-FE network to expand the receptive field and strengthen boundary feature representation; and (iii) a FFDFA mechanism leveraging distance-aware weighting to improve inter-channel feature integration.
3. Extensive experiments on two widely adopted LiDAR segmentation benchmarks demonstrate the superiority of DAGLFNet. Specifically, it achieves mean Intersection-over-Union (mIoU) scores of 69.8% and 78.7% on the SemanticKITTI and nuScenes validation sets, respectively.

2. Related Work

2.1. Methodologies for LiDAR Point Cloud Semantic Segmentation

Point cloud semantic segmentation assigns semantic labels to individual points in LiDAR scenes, transforming unstructured data into structured environmental understanding [19–21]. This section focuses on three prominent paradigms: point-based, voxel-based, and multi-modal fusion methods.

Point-based methods operate directly on raw point clouds, preserving the full spatial geometric information of the scene. PointNet [8] pioneered the application of multi-layer perceptrons (MLPs) [22] to extract global feature correlations, inspiring subsequent architectures that integrate point convolution [23, 24] to capture local spatial patterns, graph convolution [25, 26] to model neighborhood relationships, and attention mechanisms [27, 28] to focus on salient features. These methods enhance local feature extraction and geometric structure preservation capabilities. However, when processing large-scale point clouds, computational complexity remains high due to intensive computation and the lack of efficient downsampling strategies.

Voxel-based methods convert point clouds to regular 3D grids using 3D CNNs for geometric feature extraction, yet face computational burdens due to sparsity. OctNet [9] addresses this through octree decomposition to reduce redundant calculations, though still encounters bottlenecks in large-scale scenarios. To further optimize sparse grid processing, MinkNet [12] introduces Minkowski convolution operations that better capture geometric relationships in sparse voxel grids, achieving higher efficiency than traditional voxelization methods. Meanwhile, Cylinder3D [11] employs cylindrical voxelization specifically designed for LiDAR data, enabling better feature representation in cylindrical coordinates and particularly suitable for point clouds with strong structural characteristics in specific viewing angles. However, these methods face trade-offs between computational efficiency and detailed feature extraction, as rapidly increasing voxel counts in large LiDAR scenes impose significant computational overhead.

In response to the inherent limitations of single data sources in comprehensively capturing point cloud information, multi-modal fusion strategies have been developed to leverage the complementary advantages of heterogeneous input data. UniSeg [13] fuses voxel, view, and image features to fully utilize multi-modal semantic information. However, in practical applications, the

heterogeneity of data sources in coordinate systems, resolution, and temporal synchronization makes precise feature alignment a significant challenge.

2.2. 2D Representation for Semantic Segmentation

To achieve a balance between performance and efficiency in LiDAR point cloud semantic segmentation, researchers have proposed range image-based semantic segmentation methods [14–16, 30]. RangeNet++ [30] projects LiDAR point clouds onto spherical range images and applies convolutional neural networks for semantic segmentation, effectively reformulating the task into a structured two-dimensional representation. SalsaNext [31] and CENet [17] leverage enhanced contextual modeling to effectively mitigate boundary blurring and detail degradation inherent to pseudo-image-based methodologies. RangeFormer [16] partitions the entire LiDAR scan into multiple view-specific subsets and incorporates a Transformer-based architecture to capture long-range dependencies. Although these methods demonstrate reliable overall performance, they operate solely on points projected onto the image, struggle to resolve conflicts arising from multiple points mapping to the same location, overlook occluded points, and fail to preserve the full three-dimensional structure. To address this problem, FRNet [14] integrates point cloud and 2D features, preserving the fidelity of three-dimensional geometric information while leveraging the computational efficiency of two-dimensional convolutions. FARVNet [15] incorporates a reflectivity reconstruction module, amplifying the contribution of reflectivity to feature representation and thereby enhancing model robustness. Although achieving strong overall performance, these methods overlook intra-subset feature correlations, limiting their ability to accurately recognize sparsely occluded regions at long distances. Distinct from prior approaches, this work emphasizes the coherent modeling of intra-subset feature relationships while systematically accounting for the effects of spatial distance, highlighting a more holistic consideration of local and contextual dependencies.

3. Methodology

Building on the limitations identified in Section 2.2, we propose a unified framework that jointly optimizes 2D projection and 3D structural fidelity. Our framework consists of four complementary components: a GL-FFE module for capturing contextual and local geometric dependencies, a MB-FE network for enhancing boundary representations, a FFDFD strategy for precise integration of multi-scale information, and a fusion head to integrate low-level and high-level semantic information. The architecture overview of the proposed DAGLFNet framework is depicted in Fig. 2.

3.1. Problem Definition

Given a point cloud $P = \{p_1, p_2, \dots, p_N\}$, where each point $p_j = (x_j, y_j, z_j, I_j)$ consists of its 3D coordinates (x_j, y_j, z_j) and reflectivity I_j captured by the LiDAR sensor, our network aims to predict a semantic label $l_i \in L$ for each point p_j through the network architecture \mathcal{G} . Formally, the network can be defined as:

$$L = \mathcal{G}(P, \theta) \quad (1)$$

where θ represents the learnable parameters within the network. As illustrated in Fig. 2, DAGLFNet comprises four key steps: 1) a global-local point cloud feature encoder for point cloud representation; 2) an image feature encoder for extracting semantic features; 3) a point cloud feature fusion module guided by depth values via an attention mechanism; 4) a fusion head that integrates multi-level point cloud features to achieve precise semantic prediction.

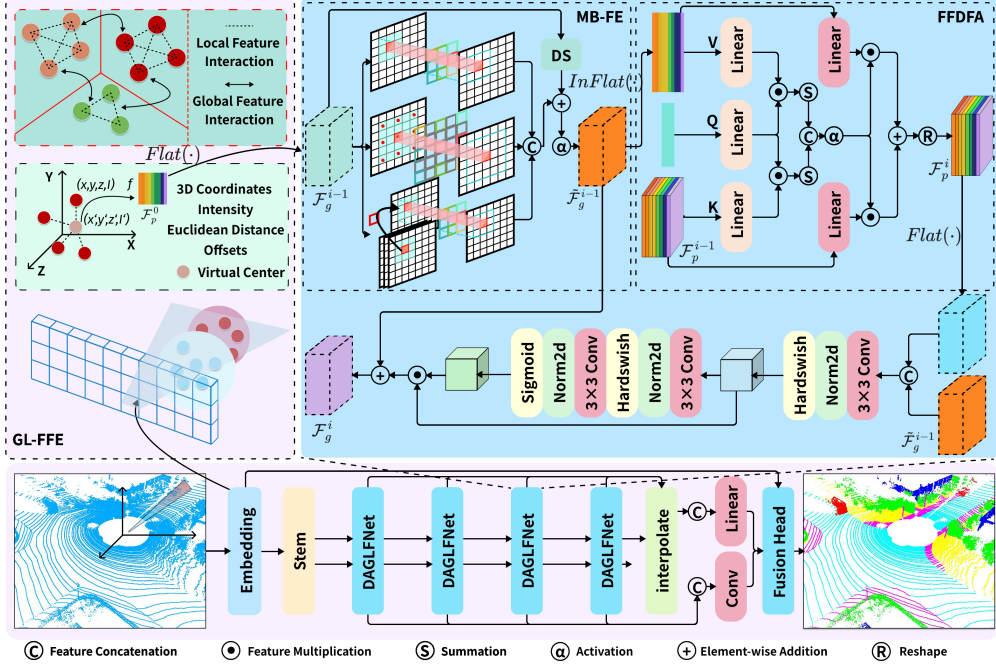


Fig. 2. The proposed DAGLFNet framework consists of key components such as GL-FFE, MB-FE, FFDDA, and the Fusion Head, which are responsible for contextual and geometric feature extraction, boundary enhancement, multi-scale feature integration, and final prediction respectively. Multiple stacked DAGLFNet units continuously learn complex hierarchical features from the point cloud, with the Fusion Head combining point-level and group-level features to predict the final output.

3.2. Feature Encoder

Given the sparsity of point cloud data [32], the design of feature encoder is crucial for effectively extracting features and converting them into 2D representations. Unlike conventional voxelization or regional partitioning approaches [11, 30], we propose a grouping strategy based on laser beam characteristics to divide the point cloud into M groups $P = \{\mathcal{P}_1, \mathcal{P}_2, \dots, \mathcal{P}_M\}$, as follows:

$$r = \sqrt{x^2 + y^2 + (z - h_l)^2}, \alpha = \text{atan}(y, x), \phi = \phi_l, \quad (2)$$

where h_l and ϕ_l denote the vertical offset and the elevation angle of the l -th laser beam, respectively. We then compute the projection coordinates of points (r, α, ϕ) as $u = ((\alpha + \pi)2\pi)W$, $v = l$, where (u, v) denotes the grid coordinate of a point in the range image with a resolution of $H \times W$.

To comprehensively capture geometric and contextual information within each group, the virtual center p_{avg} is obtained by applying average pooling over all points in the group. This center serves as a reference for encoding relative spatial relationships. The initial feature representation of each point, denoted as $\bar{p}_j \in \mathbb{R}^{1 \times 10}$, is constructed by integrating multiple complementary information sources, including absolute 3D coordinates, reflectance intensity, depth (Euclidean distance to the sensor), and relative offsets to the group center p_{avg} . This multi-modal feature encoding allows the network to learn both global context and local geometric details. The feature vector for each point is defined as:

$$\bar{p}_j = ([x_j, y_j, z_j, I_j, depth_j; p_j - p_{avg}]) \quad (3)$$

Collectively, the features of all points form the point cloud feature matrix $\bar{P} = \{\bar{p}_1, \bar{p}_2, \dots, \bar{p}_J\} \in \mathbb{R}^{N \times 10}$. Subsequently, an MLP [22] is employed to extract discriminative point cloud features. Each point feature \bar{p}_j is first encoded by an MLP, yielding the initial per-point feature representation $\mathcal{F}_p^0 \in \mathbb{R}^{N \times C}$. Although the point-level features \mathcal{F}_p^0 already encode the context of each point within the entire point cloud, they do not explicitly model the geometric relationships among points within each group. To address this, features within each group \mathcal{P}_M are aggregated to obtain compact group-level representations. Specifically, max pooling and average pooling are applied to the point-level features to capture complementary structural patterns. The resulting features are concatenated and projected through a linear mapping followed by ReLU activation, yielding the final group-level features, $\mathcal{F}_g^0 \in \mathbb{R}^{H \times W \times C}$:

$$\begin{cases} \mathcal{F}_p^0 = \text{MLP}(\bar{P}), \\ F_{\text{cat}} = [\text{MAX}(\mathcal{F}_p^0); \text{AVE}(\mathcal{F}_p^0)], \\ \mathcal{F}_g^0 = \text{Flat}(\text{ReLU}(\text{Linear}(F_{\text{cat}}))). \end{cases} \quad (4)$$

where $\text{Flat}(\cdot) : \mathbb{R}^{N \times C} \rightarrow \mathbb{R}^{H \times W \times C}$ denotes the function that maps point features onto the range image plane with resolution (H, W) . \mathcal{F}_p^0 preserves individual point characteristics, while \mathcal{F}_g^0 incorporates global contextual understanding through aggregated group-level features, forming a complementary representation.

3.3. Image Feature Extraction

We design a MB-FE network to process projected group-level features \mathcal{F}_g^{i-1} , addressing sparsity and blurred boundaries in pseudo-image representations. Following prior work [14, 16, 33], we construct the backbone using multiple convolutional blocks. Each BasicBlock serves as a core multi-branch unit capturing features at diverse receptive fields. Branch 1) employs a standard 3×3 convolution to extract local features; Branch 2) uses a dilated 3×3 convolution (dilation=2) [34] to enlarge the receptive field and capture richer contextual information; Branch 3) focuses on edge enhancement by first reducing the channel dimension with a 1×1 convolution, followed by a 3×3 convolution. Subsequently, the outputs of the three branches are concatenated along the channel dimension and fused via 1×1 convolution. The fused output is then combined with the input through a residual connection, followed by an activation function. This process can be expressed as:

$$\begin{cases} F_1 = \sigma(\text{Conv}_{3 \times 3}(\mathcal{F}_g^{i-1})), \\ F_2 = \sigma(\text{Conv}_{3 \times 3}^{d=2}(\mathcal{F}_g^{i-1})), \\ F_3 = \sigma(\text{Conv}_{3 \times 3}(\sigma(\text{Conv}_{1 \times 1}(\mathcal{F}_g^{i-1})))), \\ F_{\text{temp}} = \text{Conv}_{1 \times 1}([F_1, F_2, F_3]), \\ \tilde{\mathcal{F}}_g^{i-1} = \sigma(F_{\text{temp}} + \mathcal{F}_g^{i-1}) \end{cases} \quad (5)$$

Here, $\text{Conv}_{k \times k}$ denotes a $k \times k$ convolution, $\text{Conv}_{3 \times 3}^{d=2}$ denotes a dilated convolution with a dilation rate of 2, and $\sigma(\cdot)$ represents the normalization and activation applied after the convolution.

3.4. Feature Update Module

The input to the feature update module consists of point-level features \mathcal{F}_p^{i-1} and group-level features \mathcal{F}_g^i , where \mathcal{F}_g^i is the output of the MB-FE network from the current stage (Section 3.3). To preserve feature consistency between these representations, we integrate the local group-level features into the point-level features through a depth-guided fusion mechanism that maintains

geometric relationships and enhances discriminative power. We first project the group-level feature representation \tilde{F}_g^{i-1} into its corresponding point-level feature space \tilde{F}_p^{i-1} according to the projection index, using the operator $\text{InFlat}(\cdot) : \mathbb{R}^{H \times W \times C} \rightarrow \mathbb{R}^{N \times C}$. To enable effective cross-feature interaction in the attention mechanism, we apply linear transformations to both the projected features \tilde{F}_p^{i-1} and the original point-level features F_p^{i-1} , projecting them into a unified latent space. Unlike conventional attention mechanisms [35, 36], our approach introduces depth information as a dynamic modulation factor to adaptively refine feature weighting. The depth features $depth$ are linearly transformed to generate the query Q . This depth-guided adjustment preserves spatial coherence during feature transformation and effectively mitigates the geometric distortions that typically arise in cross-dimensional feature fusion:

$$\begin{cases} V_g, K_g = \text{Linear}(\text{InFlat}(\tilde{F}_g^{i-1})) \\ V_p, K_p = \text{Linear}(F_p^{i-1}) \\ Q = \text{Linear}(depth) \end{cases} \quad (6)$$

The \tilde{F}_g^{i-1} are projected into key and value representations, K_g and V_g , respectively, while the F_p^{i-1} are similarly transformed into K_p and V_p . The attention weights W_g and W_p are computed by measuring the similarity between the depth query Q and the corresponding keys K_g and K_p , followed by softmax normalization. These weights are then applied to their respective value matrices and aggregated to obtain the fused representation $F_{\text{fuse_}p}$. Finally, $F_{\text{fuse_}p}$ undergoes a linear transformation to produce the output feature \mathcal{F}_p^i :

$$\begin{cases} W_g = \text{softmax}(Q \odot K_g) \\ W_p = \text{softmax}(Q \odot K_p) \\ F_{\text{fuse_}p} = W_g \odot V_g + W_p \odot V_p \\ \mathcal{F}_p^i = \text{Linear}(F_{\text{fuse_}p}) \end{cases} \quad (7)$$

Given the inherent blurriness of image features, the convolutional process intrinsically degrades feature discriminability, compromising representational robustness. To counteract the degradation of image feature discriminability introduced by convolutional operations, the updated point-level features \mathcal{F}_p^i are re-projected onto the image space by $\text{Flat}(\cdot)$, concatenated with \mathcal{F}_g^{i-1} , and fused through convolutional processing:

$$\tilde{F}_{\text{fuse_}g} = \sigma(\text{Conv}_{1 \times 1}([\text{Flat}(\mathcal{F}_p^i); \tilde{F}_g^{i-1}])) \quad (8)$$

To alleviate feature degradation caused by multiple convolutional operations, the fused feature \tilde{F}_g is integrated with the global-level feature $\mathcal{F}_{\text{fuse_}g}^{i-1}$ at the current stage through a residual-attentive enhancement mechanism:

$$\mathcal{F}_g^i = \mathcal{F}_g^{i-1} + \phi(\text{Conv}_{3 \times 3}(\sigma(\text{Conv}_{3 \times 3}(\tilde{F}_{\text{fuse_}g})))) \odot \tilde{F}_{\text{fuse_}g} \quad (9)$$

where $\phi(\cdot)$ represents the normalization and the sigmoid activation applied after the convolution.

3.5. Fusion Head Module

To fully leverage the fine-grained spatial details provided by low-level features and the rich semantic context encoded in high-level features for complementary advantages, the primary task of the fusion head is to aggregate features from multiple stages. Specifically, for point-level features, the consistent topological structure across stages allows for direct feature-level concatenation, enabling the integration of multi-stage information while preserving local details and semantic cues. However, due to the downsampling operations in the backbone network, image features from different stages exhibit varying spatial resolutions. To address this issue, all

image features are resized to a consistent spatial resolution using linear interpolation to achieve spatial alignment, denoted as $\text{BilInterp}(\cdot)$:

$$\begin{cases} \mathcal{F}_p^{out} = \text{MLP}([\mathcal{F}_p^1; \dots; \mathcal{F}_p^K]) \\ \hat{\mathcal{F}}_g^i = \text{BilInterp}(\mathcal{F}_g^i, h, w), \quad i = 1, \dots, K \\ \mathcal{F}_g^{out} = \sigma(\text{Conv}([\hat{\mathcal{F}}_g^1; \dots; \hat{\mathcal{F}}_g^K])) \end{cases} \quad (10)$$

where K denotes the number of network layers, and (h, w) represents the target resolution obtained through linear interpolation. We observe that the point-level feature \mathcal{F}_p^{out} mainly contains local spatial details for describing fine structural characteristics, while the group-level feature \mathcal{F}_g^{out} integrates semantic information from a broader receptive field to represent the overall scene characteristics.

$$\mathcal{F}_{logit} = \text{MLP}(\text{MLP}(\text{InFlat}(\mathcal{F}_g^{out})) + \mathcal{F}_p^{out}) + \mathcal{F}_p^0 \quad (11)$$

Here, \mathcal{F}_{logit} is used to generate the final semantic scores with a linear head for the point over the entire point cloud.

4. Experiments

This section evaluates the robustness and efficiency of DAGLFNet. We first describe the benchmark datasets and implementation protocols. Subsequently, quantitative and qualitative experimental results demonstrate the effectiveness of DAGLFNet, highlighting its favorable balance between accuracy and computational efficiency. Comprehensive ablation studies elucidate the contribution of each network component.

4.1. Datasets

We conducted comprehensive evaluations on two widely used autonomous driving LiDAR datasets. SemanticKITTI [4], the dataset was collected using Velodyne HDL-64E sensors in Karlsruhe, Germany. It comprises 22 sequences with annotated point clouds. Sequences 0–7 and 9–10 are used for training, sequence 8 for validation, and sequences 11–21 for online testing. Each scene contains approximately 120,000 points annotated across 28 semantic categories. The vertical field of view (FoV) spans -25° to 3° . nuScenes [5], the dataset was captured using a 32-beam LiDAR. It includes 1,000 driving scenes with densely annotated point clouds across 32 classes, of which 16 categories are evaluated for semantic segmentation. The vertical field of view (FoV) ranges from -30° to 10° . These datasets provide diverse and challenging scenarios for evaluating LiDAR-based semantic segmentation methods.

4.2. Evaluation Metrics

Segmentation performance was evaluated using mean Intersection over Union (mIoU) and mean Accuracy (mAcc). For a semantic class cla , True Positives (TP_{cla}), False Positives (FP_{cla}), and False Negatives (FN_{cla}) are defined. The IoU for class cla is calculated as:

$$IoU_{cla} = \frac{TP_{cla}}{TP_{cla} + FP_{cla} + FN_{cla}}. \quad (12)$$

The mean IoU (mIoU) across all classes is computed as:

$$mIoU = \frac{1}{\text{number of classes}} \sum_{cla} IoU_{cla}. \quad (13)$$

Similarly, the per-class accuracy is defined as:

$$\text{Acc}_{cla} = \frac{TP_{cla}}{TP_{cla} + FN_{cla}}, \quad (14)$$

and the mean accuracy (mAcc) across all classes is:

$$\text{mAcc} = \frac{1}{\text{number of classes}} \sum_{cla} \text{Acc}_{cla}. \quad (15)$$

These metrics provide a comprehensive measure of segmentation quality, accounting for both overlap and class-wise correctness.

4.3. Implementation Details

Although SemanticKITTI [4] and nuScenes [5] differ in LiDAR beam count (64 vs. 32), both utilize a full 360° horizontal field of view (FoV). The range image resolutions were set to 64×1024 and 32×1024 for SemanticKITTI [4] and nuScenes [5], respectively. The optimization strategy employs the AdamW [37] optimizer with an initial learning rate of 0.001, and the OneCycle [38] policy was used for adaptive learning rate scheduling. The batch size is fixed at 4 to maintain a trade-off between efficiency and memory consumption. All experiments were conducted on a single NVIDIA RTX 4090 GPU.

4.4. Quantitative Results

We systematically compare DAGLFNet with several state-of-the-art network architectures to comprehensively evaluate performance on the SemanticKITTI [4] and nuScenes [5] datasets. The evaluation encompasses both accuracy and computational efficiency, demonstrating that DAGLFNet achieves an excellent balance between the two and exhibits outstanding overall capability.

Table 1. The class-wise IoU scores of different LiDAR semantic segmentation approaches on the SemanticKITTI [4] val set. All mIoU scores are given in percentage (%). The best and second best scores for each class are highlighted in bold and underline. † refers to test-time augmentation.

Method	mIoU	Car	Bicycle	Motorcycle	Truck	Other-vehicle	Person	Bicyclist	Motorcyclist	Road	Parking	Sidewalk	Other-ground	Building	Fence	Vegetation	Trunk	Terrain	Pole	Traffic-sign
RandLA-Net [6]	50.0	92.0	8.0	12.8	74.8	46.7	52.3	46.0	0.0	93.4	32.7	73.4	0.1	84.0	43.5	83.7	57.3	73.1	48.0	27.0
RangeNet++ [30]	51.0	89.4	26.5	48.4	33.9	26.7	54.8	69.4	0.0	92.9	37.0	69.9	0.0	83.4	51.0	83.3	54.0	68.1	49.8	34.0
SqueezeSegV2 [39]	40.8	82.7	15.1	22.7	25.6	26.9	22.9	44.5	0.0	92.7	39.7	70.7	0.1	71.6	37.0	74.6	35.8	68.1	21.8	22.2
SqueezeSegV3 [40]	53.3	87.1	34.3	48.6	47.5	47.1	58.1	53.8	0.0	95.3	43.1	78.2	0.3	78.9	53.2	82.3	55.5	70.4	46.3	33.2
SalasNet [31]	59.4	90.5	44.6	49.6	86.3	54.6	74.0	81.4	0.0	93.4	40.6	69.1	0.0	84.6	53.0	83.6	64.3	64.2	54.4	39.8
MinkowskiNet [41]	58.5	95.0	23.9	50.4	55.3	45.9	65.6	82.2	0.0	94.3	43.7	76.4	0.0	87.9	57.6	87.4	67.7	71.5	63.5	43.6
SPVNAS [42]	62.3	96.5	44.8	63.1	55.9	64.3	72.0	86.0	0.0	93.9	42.4	75.9	0.0	88.8	59.1	88.0	67.5	73.0	63.5	44.3
Cylinder3D [11]	64.9	96.4	61.5	78.2	66.3	69.8	80.8	<u>93.3</u>	0.0	94.9	41.5	78.0	1.4	87.5	55.0	86.7	72.2	68.8	63.0	42.1
PMF [43]	63.9	95.4	47.8	62.9	68.4	75.2	78.9	71.6	0.0	96.4	43.5	80.5	1.0	88.7	60.1	<u>88.6</u>	<u>72.7</u>	<u>75.3</u>	65.5	43.0
rangvit [44]	60.9	94.7	44.1	61.4	71.9	37.7	65.3	75.5	0.0	95.5	48.4	83.1	0.0	88.3	60.0	86.3	65.3	72.7	63.1	42.7
CENet [17]	61.5	91.6	42.4	61.7	82.4	63.5	64.4	76.6	0.0	93.0	50.3	72.7	0.1	85.0	54.4	84.1	61.0	70.3	55.2	42.8
RangeFormer [16]	66.5	95.0	58.1	72.1	85.1	59.8	76.9	86.4	0.2	94.8	<u>55.5</u>	81.7	<u>13.0</u>	88.5	64.5	86.5	66.8	73.0	64.0	52.0
SphereFormer [45]	67.8	96.8	51.0	75.0	93.4	64.4	77.0	92.6	0.8	94.7	53.2	52.1	3.7	90.7	58.5	88.7	71.3	75.9	64.7	54.5
FRNet [14]	67.6	97.2	53.3	72.9	81.5	72.9	77.2	90.8	0.2	95.9	53.7	83.9	9.0	90.5	65.9	87.0	66.8	72.6	64.0	47.9
waffleIron [46]	68.0	96.1	58.1	<u>79.7</u>	77.4	59.0	<u>81.1</u>	92.2	1.3	95.5	50.2	83.6	6.0	92.1	67.5	87.8	73.8	73.0	65.7	<u>52.2</u>
FARVNet [15]	68.5	97.0	54.2	75.9	89.6	72.6	76.0	90.1	0.0	95.7	56.9	83.4	22.7	89.8	62.3	87.0	65.9	73.0	63.2	47.1
DAGLFNet	<u>69.1</u>	<u>97.4</u>	58.2	78.0	89.6	<u>76.6</u>	80.5	92.3	0.0	96.0	50.1	<u>83.7</u>	0.00	91.3	<u>68.5</u>	87.9	69.5	74.1	<u>66.3</u>	51.0
DAGLFNet [†]	69.9	97.4	<u>59.9</u>	81.4	<u>90.9</u>	77.3	81.3	93.5	0.0	<u>96.2</u>	51.7	84.1	0.1	<u>91.8</u>	70.0	88.0	70.5	74.2	67.3	51.6

Table 2. The class-wise IoU scores of different LiDAR semantic segmentation approaches on the val set of nuScenes [5]. All IoU scores are given in percentage (%). The best and second best scores for each class are highlighted in bold and underline. [†] refers to test-time augmentation.

Method	mIoU	Barrier	Bicycle	Bus	Car	Construction-vehicle	Motorcycle	Pedestrian	Traffic-cone	Trailer	Truck	Driveable-surface	Other-ground	Sidewalk	Terrain	Mannmade	Vegetation
AF2S3Net [47]	62.2	60.3	12.6	82.3	80.0	20.1	62.0	59.0	49.0	42.2	67.4	94.2	68.0	64.1	68.6	82.9	82.4
RangeNet++ [30]	65.5	66.0	21.3	77.2	80.9	30.2	66.8	69.6	52.1	54.2	72.3	94.1	66.6	63.5	70.1	83.1	79.8
PolarNet [48]	71.0	74.7	28.2	85.3	90.9	35.1	77.5	71.3	58.8	57.4	76.1	96.5	71.1	74.7	74.0	87.3	85.7
PCSCNet [49]	72.0	73.3	42.2	87.8	86.1	44.9	82.2	76.1	62.9	49.3	77.3	95.2	66.9	69.5	72.3	83.7	82.5
SalsaNext [31]	72.2	74.8	34.1	85.9	88.4	42.2	72.4	72.2	63.1	61.3	76.5	96.0	70.8	71.2	71.5	86.7	84.4
SVASeg [50]	74.7	73.1	44.5	88.4	86.6	48.2	80.5	77.7	65.6	57.5	82.1	96.5	70.5	74.7	74.6	87.3	86.9
RangeViT [44]	75.2	75.5	40.7	88.3	90.1	49.3	79.3	77.2	66.3	65.2	80.0	96.4	71.4	73.8	73.8	89.9	87.2
Cylinder3D [11]	76.1	76.4	40.3	91.2	93.8	51.3	78.0	78.9	64.9	62.1	84.4	96.8	71.6	76.4	75.4	90.5	87.4
AMVNet [51]	76.1	79.8	32.4	82.2	86.4	62.5	81.9	75.3	72.3	83.5	65.1	97.4	67.0	78.8	74.6	<u>90.8</u>	87.9
RPVNet [52]	77.6	78.2	43.4	92.7	<u>93.2</u>	49.0	85.7	80.5	66.0	66.9	84.0	96.9	73.5	75.9	70.6	90.6	<u>88.9</u>
WaffleIron [46]	77.6	78.7	51.3	93.6	88.2	47.2	86.5	<u>81.7</u>	68.9	69.3	83.1	96.9	74.3	75.6	74.2	87.2	85.2
RangeFormer [16]	78.1	78.0	45.2	94.0	92.9	58.7	83.9	77.9	69.1	63.7	85.6	96.7	74.5	75.1	75.3	89.1	87.5
SphereFormer [45]	<u>78.4</u>	77.7	43.8	<u>94.5</u>	93.1	52.4	<u>86.9</u>	81.2	65.4	<u>73.4</u>	85.3	97.0	73.4	75.4	75.0	91.0	89.2
WaffleAndRange [53]	77.6	78.5	<u>49.6</u>	91.8	87.6	52.7	86.7	82.2	70.1	67.2	79.7	97.0	74.7	<u>76.8</u>	74.9	87.5	85.0
FRNet [14]	76.1	77.2	39.5	93.4	88.6	52.1	81.4	75.1	65.7	66.2	79.7	96.8	75.3	75.4	75.9	88.4	85.4
FARVNet [15]	77.8	77.8	42.1	94.5	91.8	54.9	84.5	77.0	66.7	70.2	<u>85.4</u>	97.0	74.6	76.4	75.9	89.2	87.4
DAGLFNet	78.3	78.5	46.5	89.3	90.7	57.1	88.9	79.3	70.3	69.7	83.1	97.0	<u>75.9</u>	76.1	<u>76.0</u>	89.9	88.2
DAGLFNet [†]	78.7	<u>78.8</u>	47.1	89.7	90.4	<u>57.4</u>	86.8	80.4	<u>71.1</u>	70.6	81.9	<u>97.0</u>	76.5	76.4	76.2	90.0	88.4

The results presented in Tables 1 and 2 demonstrate the competitive performance of DAGLFNet. The results demonstrate that DAGLFNet significantly outperforms previous methods across most category-level metrics. On the SemanticKITTI [4] validation set, DAGLFNet achieves an mIoU of 69.1%, surpassing WaffleIron [46] by 1.1% and FARVNet [14] by 0.6%. On the nuScenes [5] validation set, it achieves 78.3%, outperforming WaffleAndRange [53] by 0.7% and FARVNet [15] by 0.5%, ranking among the top performers across multiple categories.

The proposed GL-FFE, MB-FE, and FFDDFA modules collectively achieve significant performance gains over the baseline, establishing DAGLFNet superiority in handling complex and sparse point clouds. Fig. 3 validates this overall advantage through consistent improvements across dynamic and static classes, with the truck category showing a 23% IoU gain that directly reflects the efficacy of GL-FFE and MB-FE in stabilizing local features and enhancing boundary discrimination for irregular structures. Fig. 4 further demonstrates module utility under extreme conditions, where the 12.5% mIoU gain at the 40–45m range specifically proves FFDDFA effectiveness in leveraging depth information to prioritize valid structural features while suppressing noise in sparse regions. These results collectively confirm the critical role of all three modules in enabling robust segmentation across diverse challenging scenarios.

Fig. 5 illustrates the relationship between mIoU and inference speed (ms/scan) on the SemanticKITTI [4] validation set for several state-of-the-art point cloud semantic segmentation methods. Our method, DAGLFNet, achieves the highest 69.1% mIoU while maintaining a moderate inference speed of 45.4 ms/scan, striking an optimal balance between accuracy and efficiency. Methods like FRNet [14] and FARVNet [15] exhibit slightly lower accuracy with comparable inference speeds, whereas faster methods such as CENet [17] achieve very low latency

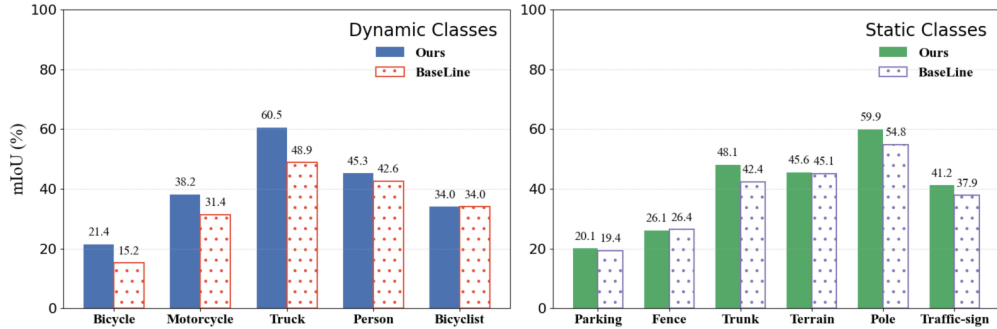


Fig. 3. Class-wise LiDAR segmentation results of DAGLFNet and the baseline model on the val set of SemanticKITTI [4].

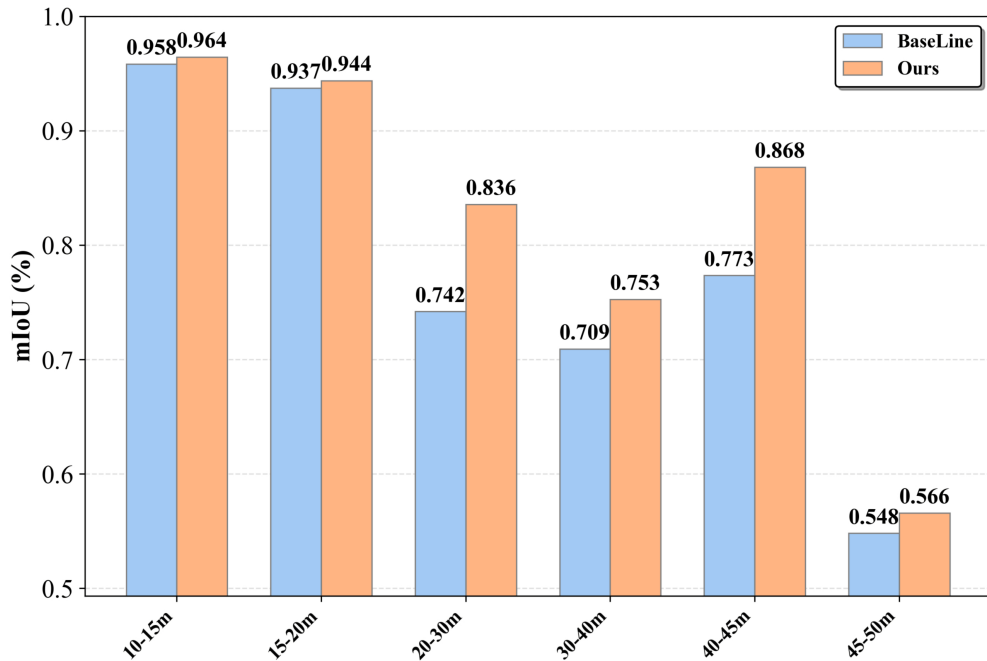


Fig. 4. Comparison of mIoU (%) between DAGLFNet and the baseline method across different distance ranges.

(7.6 ms/scan) but with significantly lower accuracy (61.5% mIoU). Similarly, WaffleIron [46] shows fast inference but slightly reduced accuracy. Overall, DAGLFNet demonstrates a well-balanced trade-off between accuracy, inference efficiency, and model complexity.

4.5. Qualitative Results

Fig. 6 visualizes segmentation errors in challenging scenes from the SemanticKITTI [4] validation set. We examine four specific scenarios: (a) For large-scale vegetation point clouds, other methods struggle to extract the most discriminative features, leading to extensive segmentation errors. In contrast, DAGLFNet accurately segments most complex regions, outperforming others significantly. (b) Furthermore, in occluded areas of similar scenes, DAGLFNet maintains accurate classification of vegetation within the occluded regions, showcasing its effectiveness

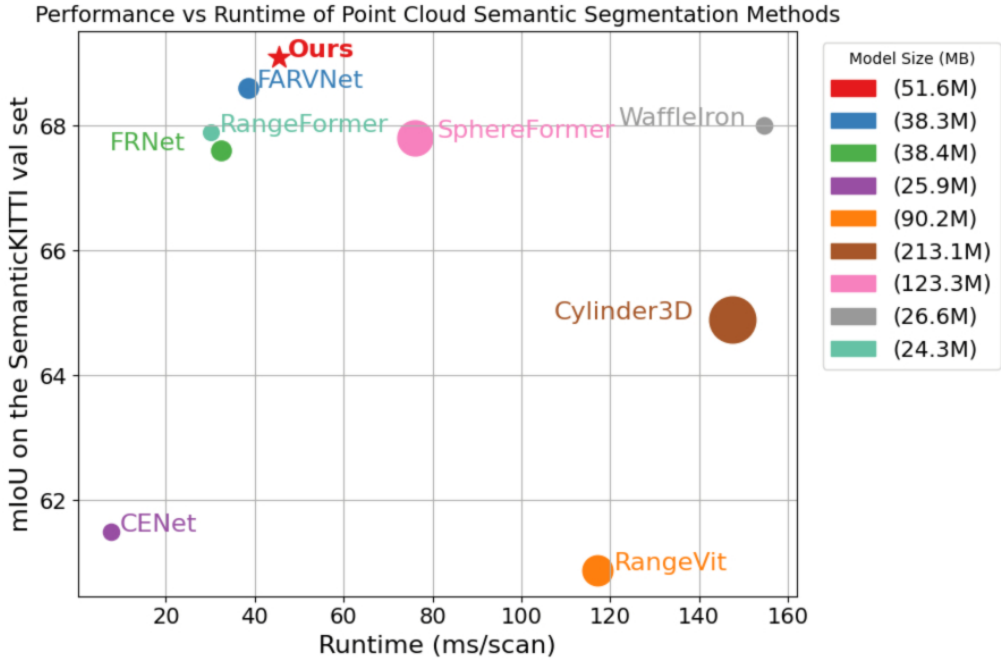


Fig. 5. mIoU vs. inference speed for various point cloud semantic segmentation methods on the SemanticKITTI [4] validation set. Marker size indicates model size. DAGLFNet achieves the best balance of accuracy and speed.

in local feature recognition. (c) In complex intersection scenarios—characterized by numerous and diverse categories—road recognition is critical. However, methods like SphereFormer [16] and WaffleIron [46] fail to classify roads correctly, whereas DAGLFNet accurately identifies them, ensuring precise scene understanding. (d) Obstacle recognition, particularly vehicles at intersections, is equally crucial. Other methods perform poorly when identifying vehicles near turning intersections, while DAGLFNet demonstrates more robust and reliable recognition capabilities.

To further investigate segmentation errors, we visualize three challenging scenarios in Fig. 7: (a) narrow sidewalks, (b) occlusion cases, and (c) complex interactions involving vegetation, terrain, and occlusions. In these scenes, existing methods exhibit critical limitations: WaffleIron [46], FARVNet [15], and FRNet [14] misclassify sidewalks as terrain (a); FRNet [14] and FARVNet [15] incorrectly label occluded roads as sidewalks, while WaffleIron [46] inconsistently segments overlapping regions (b); and all struggle to distinguish intertwined vegetation from terrain (c). In contrast, DAGLFNet uniquely resolves these challenges, achieving correct segmentation of narrow sidewalks, robust handling of occlusion ambiguities, and precise separation of vegetation-terrain boundaries. These consistent failures across methods stem from a fundamental limitation: they process all points within projection subsets uniformly, regardless of distance. Consequently, noise from distant points dominates feature representations, obscuring critical geometric details in proximity and causing systematic misclassification.

To further evaluate the performance of DAGLFNet in distant sparse regions, we compared the segmentation of vehicles and buses, as shown in Fig. 8. In distant sparse point clouds, FARVNet [15] and FRNet [14] tend to confuse sparse vehicles with adjacent sparse terrain, resulting in cars being misclassified as terrain. Under distant occlusion conditions, FARVNet [15] misclassifies buses as background buildings, while FRNet [14] only partially recognizes them

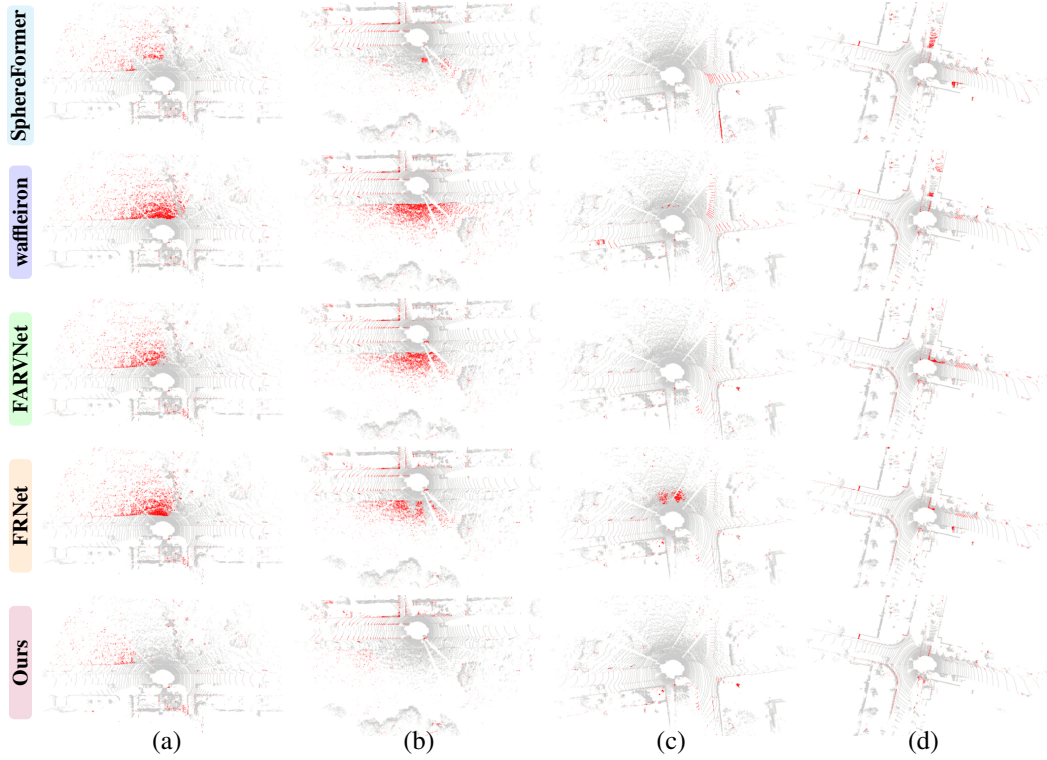


Fig. 6. Segmentation errors in challenging scenes on the SemanticKITTI [4] validation set. Red represents misclassified areas, and gray represents correctly classified areas. The four representative scenarios include: (a) segmentation of large-scale vegetation point clouds; (b) classification of vegetation in occluded regions; (c) road recognition in complex intersections; and (d) identification of vehicles and obstacles at intersections. DAGLF-Net demonstrates higher accuracy and robustness across all scenarios.

and still confuses them with the background. This is mainly because conventional methods do not fully exploit global context and multi-scale features when processing sparse point clouds and local information. In contrast, DAGLFNet combines local and global features, enhances contextual information, aligns multi-scale features, and integrates a depth-guided attention mechanism, enabling distant and occluded targets to be more effectively distinguished and recognized, thereby achieving higher robustness and accuracy.

4.6. Ablation Study

In this section, we discuss the effectiveness of each design component in the DAGLFNet architecture. All experiments are conducted and reported separately on the validation sets of SemanticKITTI [4] and nuScenes [5].

By introducing GL-FFE, which integrates global and local contextual information to enrich point feature representation, the model achieves an improvement of 0.5 mIoU on SemanticKITTI [4] and 0.2 mIoU on nuScenes [5]. This indicates that capturing both global scene context and local details helps to better distinguish complex structures in sparse point clouds. Subsequently, adding MB-FE, which extracts multi-scale and diverse semantic features through parallel branches, further increases mIoU by 0.4 on SemanticKITTI [4] and 0.8 on nuScenes [5], suggesting that the multi-branch design enables more comprehensive feature extraction across varying object

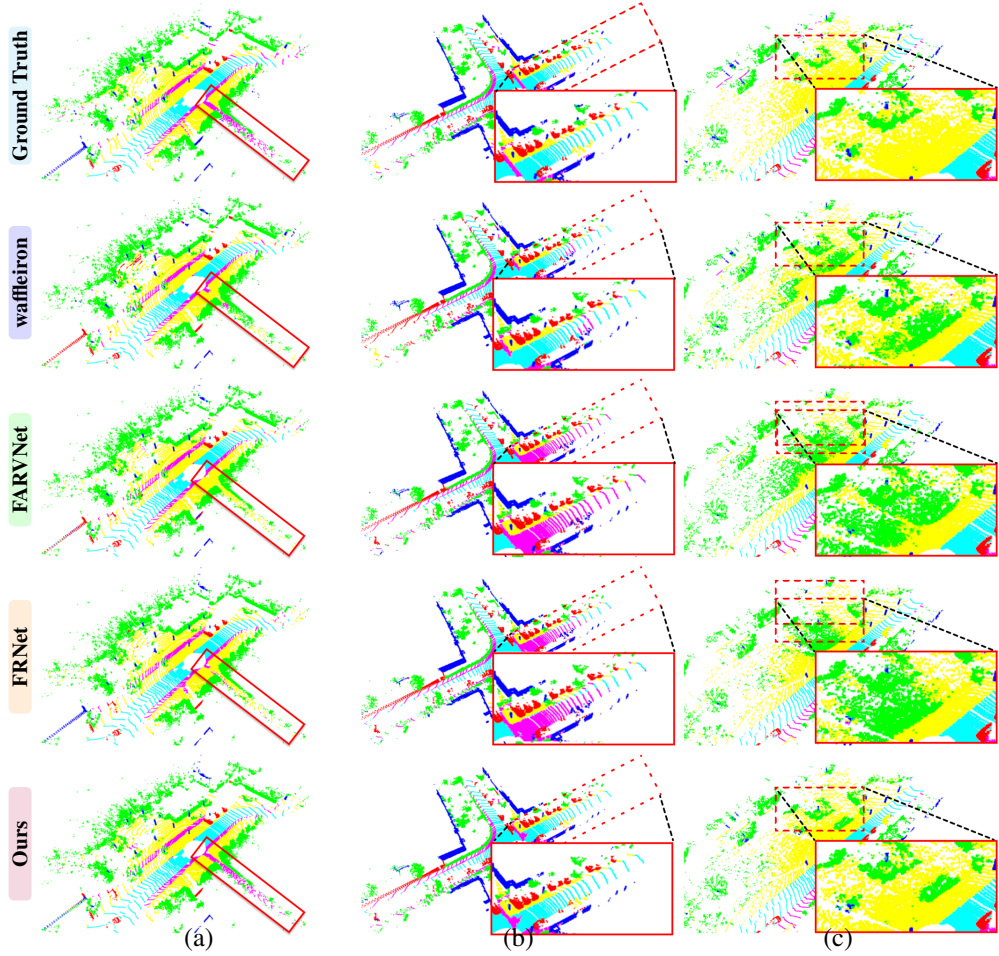


Fig. 7. Three challenging segmentation error scenarios: (a) narrow sidewalks; (b) interference cases; (c) multiple interferences including vegetation, terrain, and occlusions.

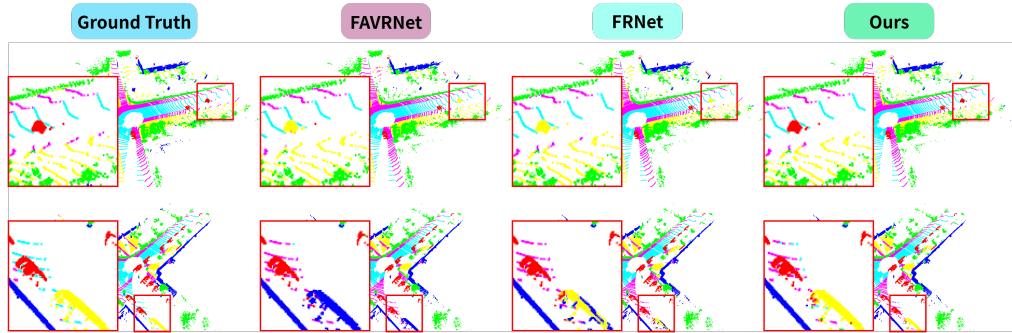


Fig. 8. Qualitative comparison of segmentation performance by different methods in distant, sparse, and occluded scenarios.

scales. Finally, the FFDDA module, leveraging attention guided by deep features to selectively enhance informative points while suppressing background noise, contributes an additional 0.9

Table 3. Ablation study of each component in Ours on the val set of SemanticKITTI [4] and nuScenes [5]. BL: BaseLine; GL-FFE: Global-Local Feature Fusion Encoding; MB-FE: Multi-Branch Feature Extraction; FFDFa: Feature Fusion via Deep Feature-guided Attention; TTA: Test Time Augmentation. All mIoU and mAcc scores are given in percentage (%).

BL	GL-FFE	MB-FE	FFDFa	TTA	SemKITTI		nuScenes	
					mIoU	mAcc	mIoU	mAcc
✓					67.3	74.0	76.1	83.9
✓	✓				67.8	74.4	76.3	84.9
✓	✓	✓			68.2	74.8	77.1	85.0
✓	✓	✓	✓		69.1	75.1	78.3	85.5
✓	✓	✓	✓	✓	69.9	75.5	78.7	85.7

mIoU on SemanticKITTI [4] and 1.2 mIoU on nuScenes [5], demonstrating its effectiveness in emphasizing critical features and improving segmentation accuracy in challenging regions. Finally, adopting test time augmentation during inference, following prior works, brings an improvement of 0.8% and 0.4% mIoU, respectively.

Table 4. Ablation of network depth: Evaluation of different depth configurations on the SemanticKITTI [4] validation set. All mIoU scores are reported in percentage (%).

Depth	mIoU	FPS	Params	Car	Bicycle	Motorcycle	Truck	Other-vehicle	Person	Bicyclist	Motorcyclist	Road	Parking	Sidewalk	Other-ground	Building	Fence	Vegetation	Trunk	Terrain	Pole	Traffic-sign
[1, 1, 1, 1]	66.1	32	28.2M	95.6	51.1	70.9	81.5	62.6	80.0	86.9	0.0	95.2	47.4	83.0	0.1	89.1	58.0	86.8	67.9	71.3	64.4	50.7
[2, 2, 2, 2]	66.9	27	36.0M	96.5	54.0	70.9	80.5	64.9	77.61	89.5	0.1	95.8	52.0	83.4	10.4	89.8	64.0	86.0	67.6	71.0	64.7	50.8
[3, 3, 3, 3]	68.3	24	43.8M	96.9	54.6	75.3	88.4	72.0	76.2	91.3	0.1	95.7	56.7	83.5	14.3	89.8	62.7	86.9	64.6	72.8	63.1	47.1
[3, 4, 6, 3]	69.1	21	51.6M	97.4	58.2	78.0	89.6	76.6	80.5	92.3	0.0	96.0	50.1	83.7	0.00	91.3	68.5	87.9	69.5	74.1	66.3	51.0

Range Image Representation. We investigate the effect of range image resolution on DAGLFNet performance. As the resolution decreases, the projected range images become coarser, causing a loss of fine-grained details in the point cloud representation. This reduction primarily affects the accurate extraction of local features and reduces segmentation accuracy for small or distant objects. In contrast, higher resolutions preserve more spatial details, enhance feature extraction, and improve segmentation performance, especially in sparse or complex regions. However, excessively high resolutions increase computational costs, while the performance gains remain limited. As shown in Table 5, we compare the results under different range image resolutions, and the configuration of 64×1024 achieves the best balance between performance and efficiency.

Network Depth. To investigate the influence of network depth on model performance, we conduct an ablation study using different depth configurations of the proposed network, denoted as [1, 1, 1, 1], [2, 2, 2, 2], [3, 3, 3, 3], and [3, 4, 6, 3]. As shown in Table 4, increasing network depth generally improves segmentation accuracy (mIoU), while slightly reducing inference speed (FPS) and increasing the number of parameters. The configuration [3, 4, 6, 3] achieves the best balance between accuracy and computational efficiency, demonstrating the effectiveness of deeper hierarchical feature extraction in our model.

Table 5. Ablation of range image resolution: Evaluation of the impact of different range image resolutions on model performance using the SemanticKITTI [4] validation set.

Image Resolution	mIoU	FPS	Car	Bicycle	Motorcycle	Truck	Other-vehicle	Person	Bicyclist	Motorcyclist	Road	Parking	Sidewalk	Other-ground	Building	Fence	Vegetation	Trunk	Terrain	Pole	Traffic-sign
64 × 256	65.8	30	95.1	50.0	67.4	82.7	55.7	65.3	87.6	0.0	95.0	64.7	83.3	24.7	88.1	60.6	88.8	61.2	79.1	55.8	45.7
64 × 512	68.2	26	96.9	54.3	75.7	71.3	77.1	75.1	91.1	0.0	95.6	63.6	84.3	14.3	90.3	66.5	88.1	66.7	75.1	61.6	48.8
64 × 768	68.0	23	96.7	51.7	79.7	92.2	69.5	77.4	85.2	0.0	95.7	47.3	83.5	10.0	90.9	66.3	87.1	61.6	72.6	66.2	50.3
64 × 1024	69.1	21	97.4	58.2	78.0	89.6	76.6	80.5	92.3	0.0	96.0	50.1	83.7	0.0	91.3	68.5	87.9	69.5	74.1	66.3	51.0
64 × 1280	68.6	17	96.2	54.7	77.2	82.2	68.4	79.6	90.0	0.0	94.9	51.6	84.0	0.0	91.3	68.8	87.6	68.3	73.1	64.6	51.7

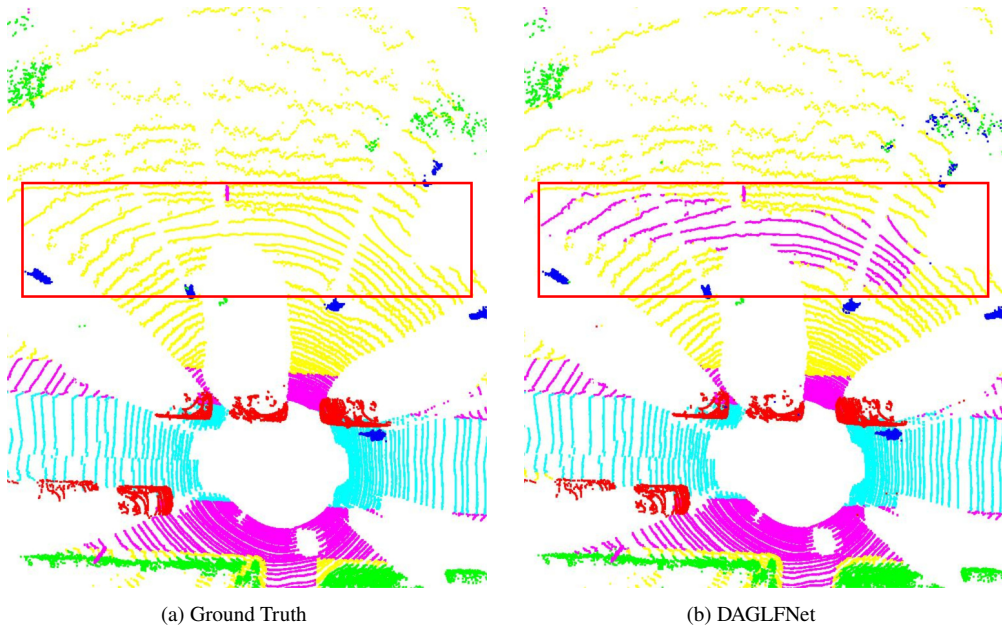


Fig. 9. Challenging cases in sparse and occluded regions. (a) Ground Truth; (b) prediction results of DAGLFNet. In areas with sparse LiDAR points and occlusions, DAGLFNet struggles to accurately distinguish highly similar ground contours and sidewalks, highlighting its limited capability in recognizing local features when dense point cloud information is lacking.

4.7. Failure Cases

We identify a primary limitation of our model in sparse and occluded regions when analyzing its performance in specific scenarios. As illustrated in Figure 9, when the LiDAR point cloud becomes sparse due to occlusion and contains large empty areas, DAGLFNet struggles to correctly recognize and distinguish semantically similar terrain contours and sidewalks. This occurs mainly because, in regions with insufficient point information, the model lacks sufficiently dense local geometric features to serve as reliable discriminative cues, leading to the misclassification of ambiguous boundaries and similar structures. These findings suggest that in environments with severe sparsity or occlusion, the robustness of fine-grained geometric and semantic contextual understanding still needs further enhancement.

5. Conclusion

In this work, we introduce DAGLFNet, a pseudo-image-based framework for point cloud semantic segmentation, specifically engineered to mitigate challenges arising from point cloud sparsity and occlusions. By fusing local and global features, employing a multi-branch feature extraction mechanism, and utilizing deep feature-guided attention fusion, DAGLFNet achieves robust segmentation performance in long-range, sparse, and complex environments. Comprehensive evaluations on benchmark datasets—including SemanticKITTI and nuScenes—demonstrate that the network attains competitive accuracy while preserving real-time efficiency and suitability for edge deployment.

However, DAGLFNet exhibits limitations in regions of extreme sparsity or heavy occlusion, where it may misclassify semantically similar structures such as terrain and sidewalks. This underscores the need for enhanced modeling of fine-grained geometric and semantic context in challenging environments.

Overall, DAGLFNet delivers efficient and accurate segmentation for sparse and complex point clouds, striking a balance between real-time performance and embedded deployment capabilities. Future work should prioritize improving the network’s understanding of geometric and semantic context in highly sparse and occluded areas to further enhance robustness and accuracy in complex scenarios.

Funding. Key R&D Project of the Sichuan Provincial Department of Science and Technology—Research on Three-Dimensional Multi-Resolution Intelligent Map Construction Technology (2024YFG0009), the Intelligent Identification and Assessment for Disaster Scenes: Key Technology Research and Application Demonstration (2025YFNH0008), Project of the Sichuan Provincial Department of Science and Technology—Application and Demonstration of Intelligent Fusion Processing of Laser Imaging Radar Data (2024ZHCG0176), the "Juyuan Xingchuan" Project of Central Universities and Research Institutes in Sichuan—High-Resolution Multi-Wavelength Lidar System and Large-Scale Industry Application(2024ZHCG0190), the Sichuan Science and Technology Program, Research on Simulator Three-Dimensional View Modeling Technology and Database Matching and Upgrading Methods, and the Key Laboratory of Civil Aviation Flight Technology and Flight Safety (FZ2022KF08).

References

1. H. Wang, J. Li, Y. Cai, *et al.*, “Lidar-pdp: A lidar-based panoptic dynamic driving environment perception algorithm,” *IEEE Trans. on Transp. Electrification* **11**, 1848–1862 (2025).
2. S. Li, Y. Liu, and J. Gall, “Rethinking 3-d lidar point cloud segmentation,” *IEEE Trans. on Neural Networks Learn. Syst.* **36**, 4079–4090 (2025).
3. F. Sánchez-García, S. Montiel-Marín, M. Antunes-García, *et al.*, “Salsanext+: A multimodal-based point cloud semantic segmentation with range and rgb images,” *IEEE Access* **13**, 64133–64147 (2025).
4. J. Behley, M. Garbade, A. Milioto, *et al.*, “SemanticKITTI: A dataset for semantic scene understanding of lidar sequences,” in *Proceedings of the IEEE/CVF international conference on computer vision*, (2019), pp. 9297–9307.
5. W. K. Fong, R. Mohan, J. V. Hurtado, *et al.*, “Panoptic nuscenes: A large-scale benchmark for lidar panoptic segmentation and tracking,” *IEEE Robotics Autom. Lett.* **7**, 3795–3802 (2022).

6. Q. Hu, B. Yang, L. Xie, *et al.*, “Randla-net: Efficient semantic segmentation of large-scale point clouds,” in *Proceedings of the IEEE/CVF conference on computer vision and pattern recognition*, (2020), pp. 11108–11117.
7. H. Thomas, C. R. Qi, J.-E. Deschaud, *et al.*, “Kpconv: Flexible and deformable convolution for point clouds,” in *2019 IEEE/CVF International Conference on Computer Vision (ICCV)*, (2019), pp. 6410–6419.
8. C. R. Qi, H. Su, K. Mo, and L. J. Guibas, “Pointnet: Deep learning on point sets for 3d classification and segmentation,” in *Proceedings of the IEEE conference on computer vision and pattern recognition*, (2017), pp. 652–660.
9. G. Riegler, A. Osman Ulusoy, and A. Geiger, “Octnet: Learning deep 3d representations at high resolutions,” in *Proceedings of the IEEE conference on computer vision and pattern recognition*, (2017), pp. 3577–3586.
10. H. Tang, Z. Liu, S. Zhao, *et al.*, “Searching efficient 3d architectures with sparse point-voxel convolution,” in *Computer Vision – ECCV 2020*, A. Vedaldi, H. Bischof, T. Brox, and J.-M. Frahm, eds. (Springer International Publishing, Cham, 2020), pp. 685–702.
11. H. Zhou, X. Zhu, X. Song, *et al.*, “Cylinder3d: An effective 3d framework for driving-scene lidar semantic segmentation,” arXiv preprint arXiv:2008.01550 (2020).
12. C. Choy, J. Gwak, and S. Savarese, “4d spatio-temporal convnets: Minkowski convolutional neural networks,” in *2019 IEEE/CVF Conference on Computer Vision and Pattern Recognition (CVPR)*, (2019), pp. 3070–3079.
13. Y. Liu, R. Chen, X. Li, *et al.*, “Uniseg: A unified multi-modal lidar segmentation network and the openpcseg codebase,” in *Proceedings of the IEEE/CVF International Conference on Computer Vision*, (2023), pp. 21662–21673.
14. X. Xu, L. Kong, H. Shuai, and Q. Liu, “Frnet: Frustum-range networks for scalable lidar segmentation,” arXiv preprint arXiv:2312.04484 (2023).
15. C. Chen, L. Zhao, W. Guo, *et al.*, “Farvnet: A fast and accurate range-view-based method for semantic segmentation of point clouds,” *Sensors* **25** (2025).
16. L. Kong, Y. Liu, R. Chen, *et al.*, “Rethinking range view representation for lidar segmentation,” in *Proceedings of the IEEE/CVF International Conference on Computer Vision*, (2023), pp. 228–240.
17. H.-X. Cheng, X.-F. Han, and G.-Q. Xiao, “Cenet: Toward concise and efficient lidar semantic segmentation for autonomous driving,” in *2022 IEEE international conference on multimedia and expo (ICME)*, (IEEE, 2022), pp. 01–06.
18. Y. Zhao, L. Bai, and X. Huang, “Fidnet: Lidar point cloud semantic segmentation with fully interpolation decoding,” in *2021 IEEE/RSJ International Conference on Intelligent Robots and Systems (IROS)*, (2021), pp. 4453–4458.
19. B. Gao, Y. Pan, C. Li, *et al.*, “Are we hungry for 3d lidar data for semantic segmentation? a survey of datasets and methods,” *IEEE Trans. on Intell. Transp. Syst.* **23**, 6063–6081 (2022).
20. Y. Zhao, X. Zhang, and X. Huang, “A technical survey and evaluation of traditional point cloud clustering methods for lidar panoptic segmentation,” in *2021 IEEE/CVF International Conference on Computer Vision Workshops (ICCVW)*, (2021), pp. 2464–2473.
21. S. Neshev, K. Tonchev, A. Manolova, and V. Poulikov, “3d scene segmentation: A comprehensive survey and open problems,” *IEEE Access* **13**, 110457–110496 (2025).
22. W. Zhang, Z. Yin, Z. Sheng, *et al.*, “Graph attention multi-layer perceptron,” in *Proceedings of the 28th ACM SIGKDD Conference on Knowledge Discovery and Data Mining*, (2022), pp. 4560–4570.
23. Z. Zhang, B.-S. Hua, and S.-K. Yeung, “Shellnet: Efficient point cloud convolutional neural networks using concentric shells statistics,” in *2019 IEEE/CVF International Conference on Computer Vision (ICCV)*, (2019), pp. 1607–1616.
24. M. Xu, R. Ding, H. Zhao, and X. Qi, “Paconv: Position adaptive convolution with dynamic kernel assembling on point clouds,” in *2021 IEEE/CVF Conference on Computer Vision and Pattern Recognition (CVPR)*, (2021), pp. 3172–3181.
25. G. Qian, A. Abualshour, G. Li, *et al.*, “Pu-gen: Point cloud upsampling using graph convolutional networks,” in *2021 IEEE/CVF Conference on Computer Vision and Pattern Recognition (CVPR)*, (2021), pp. 11678–11687.
26. M. Wei, Z. Wei, H. Zhou, *et al.*, “Agconv: Adaptive graph convolution on 3d point clouds,” *IEEE Trans. on Pattern Anal. Mach. Intell.* **45**, 9374–9392 (2023).
27. V. Vanian, G. Zamanakos, and I. Pratikakis, “Improving performance of deep learning models for 3d point cloud semantic segmentation via attention mechanisms,” *Comput. & Graph.* **106**, 277–287 (2022).
28. Y. Li and J. Cai, “Point cloud classification network based on self-attention mechanism,” *Comput. Electr. Eng.* **104**, 108451 (2022).
29. G. Riegler, A. Osman Ulusoy, and A. Geiger, “Octnet: Learning deep 3d representations at high resolutions,” in *Proceedings of the IEEE conference on computer vision and pattern recognition*, (2017), pp. 3577–3586.
30. A. Milioto, I. Vizzo, J. Behley, and C. Stachniss, “Rangenet++: Fast and accurate lidar semantic segmentation,” in *2019 IEEE/RSJ international conference on intelligent robots and systems (IROS)*, (IEEE, 2019), pp. 4213–4220.
31. E. E. Aksoy, S. Baci, and S. Cavdar, “Salsanet: Fast road and vehicle segmentation in lidar point clouds for autonomous driving,” in *2020 IEEE intelligent vehicles symposium (IV)*, (IEEE, 2020), pp. 926–932.
32. Q. Hu, Z. Zhang, and W. Hu, “Rangeldm: Fast realistic lidar point cloud generation,” in *Computer Vision – ECCV 2024*, (Springer Nature Switzerland, Cham, 2025), pp. 115–135.
33. C. Liu, X. Wan, and G. Gao, “A multi-branch feature extraction residual network for lightweight image super-resolution,” *Mathematics* **12** (2024).
34. F. Yu and V. Koltun, “Multi-scale context aggregation by dilated convolutions,” in *4th International Conference on Learning Representations, ICLR 2016, San Juan, Puerto Rico, May 2-4, 2016, Conference Track Proceedings*, Y. Bengio and Y. LeCun, eds. (2016).

35. X. Liu, L. Qi, Y. Song, and Q. Wen, “Depth awakens: A depth-perceptual attention fusion network for rgb-d camouflaged object detection,” *Image Vis. Comput.* **143**, 104924 (2024).

36. Z. Wu, G. Allibert, F. Meriaudeau, *et al.*, “Hidanet: Rgb-d salient object detection via hierarchical depth awareness,” *IEEE Trans. on Image Process.* **32**, 2160–2173 (2023).

37. I. Loshchilov and F. Hutter, “Decoupled weight decay regularization,” *Learning, Learning* (2017).

38. L. N. Smith and N. Topin, “Super-convergence: Very fast training of neural networks using large learning rates,” in *Artificial Intelligence and Machine Learning for Multi-Domain Operations Applications*, (2019).

39. B. Wu, X. Zhou, S. Zhao, *et al.*, “Squeezesegv2: Improved model structure and unsupervised domain adaptation for road-object segmentation from a lidar point cloud,” in *2019 international conference on robotics and automation (ICRA)*, (IEEE, 2019), pp. 4376–4382.

40. C. Xu, B. Wu, Z. Wang, *et al.*, “Squeezesegv3: Spatially-adaptive convolution for efficient point-cloud segmentation,” in *Computer Vision–ECCV 2020: 16th European Conference, Glasgow, UK, August 23–28, 2020, Proceedings, Part XXVIII 16*, (Springer, 2020), pp. 1–19.

41. C. Choy, J. Gwak, and S. Savarese, “4d spatio-temporal convnets: Minkowski convolutional neural networks,” in *Proceedings of the IEEE/CVF conference on computer vision and pattern recognition*, (2019), pp. 3075–3084.

42. H. Tang, Z. Liu, S. Zhao, *et al.*, “Searching efficient 3d architectures with sparse point-voxel convolution,” in *European conference on computer vision*, (Springer, 2020), pp. 685–702.

43. Z. Zhuang, R. Li, K. Jia, *et al.*, “Perception-aware multi-sensor fusion for 3d lidar semantic segmentation,” in *Proceedings of the IEEE/CVF International Conference on Computer Vision*, (2021), pp. 16280–16290.

44. A. Ando, S. Gidaris, A. Bursuc, *et al.*, “Rangevit: Towards vision transformers for 3d semantic segmentation in autonomous driving,” in *Proceedings of the IEEE/CVF conference on computer vision and pattern recognition*, (2023), pp. 5240–5250.

45. X. Lai, Y. Chen, F. Lu, *et al.*, “Spherical transformer for lidar-based 3d recognition,” in *Proceedings of the IEEE/CVF Conference on Computer Vision and Pattern Recognition*, (2023), pp. 17545–17555.

46. G. Puy, A. Boulch, and R. Marlet, “Using a waffle iron for automotive point cloud semantic segmentation,” in *Proceedings of the IEEE/CVF International Conference on Computer Vision*, (2023), pp. 3379–3389.

47. R. Cheng, R. Razani, E. Taghavi, *et al.*, “2-s3net: Attentive feature fusion with adaptive feature selection for sparse semantic segmentation network,” in *Proceedings of the IEEE/CVF conference on computer vision and pattern recognition*, (2021), pp. 12547–12556.

48. Y. Zhang, Z. Zhou, P. David, *et al.*, “Polarnet: An improved grid representation for online lidar point clouds semantic segmentation,” in *Proceedings of the IEEE/CVF conference on computer vision and pattern recognition*, (2020), pp. 9601–9610.

49. J. Park, C. Kim, S. Kim, and K. Jo, “Pscnet: Fast 3d semantic segmentation of lidar point cloud for autonomous car using point convolution and sparse convolution network,” *Expert Syst. with Appl.* **212**, 118815 (2023).

50. L. Zhao, S. Xu, L. Liu, *et al.*, “Svaseg: Sparse voxel-based attention for 3d lidar point cloud semantic segmentation,” *Remote. Sens.* **14**, 4471 (2022).

51. V. E. Liong, T. N. T. Nguyen, S. Widjaja, *et al.*, “Amvnet: Assertion-based multi-view fusion network for lidar semantic segmentation,” *arXiv preprint arXiv:2012.04934* (2020).

52. J. Xu, R. Zhang, J. Dou, *et al.*, “Rpnet: A deep and efficient range-point-voxel fusion network for lidar point cloud segmentation,” in *Proceedings of the IEEE/CVF international conference on computer vision*, (2021), pp. 16024–16033.

53. D. Fusaro, S. Mosco, E. Menegatti, and A. Pretto, “Exploiting local features and range images for small data real-time point cloud semantic segmentation,” in *2024 IEEE/RSJ International Conference on Intelligent Robots and Systems (IROS)*, (IEEE, 2024), pp. 4980–4987.